Journal Pre-proof

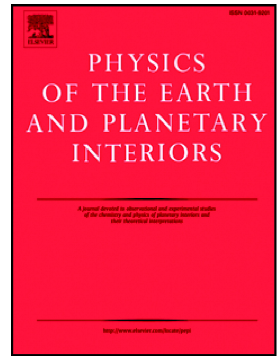

The simulation of rupture dynamics from potential earthquakes around XiLuoDu reservoir dam, China

Liao Li, Li Pingen, Yang Jiansi, Feng Jianzhou

PII: S0031-9201(19)30296-1

DOI: https://doi.org/10.1016/j.pepi.2020.106488

Reference: PEPI 106488

To appear in: *Physics of the Earth and Planetary Interiors*

Received date: 12 November 2019

Revised date: 17 March 2020

Accepted date: 31 March 2020

Please cite this article as: L. Li, L. Pingen, Y. Jiansi, et al., The simulation of rupture dynamics from potential earthquakes around XiLuoDu reservoir dam, China, *Physics of the Earth and Planetary Interiors* (2020), https://doi.org/10.1016/j.pepi.2020.106488

The Simulation of Rupture Dynamics from Potential Earthquakes around XiLuoDu reservoir dam, China

Liao Li[1]*, Li Pingen[1], Yang Jiansi[1], Feng Jianzhou[1]
1. Institute of Geophysics, China Earthquake Administration, Beijing, China,
*Correspondence: liaoli@cea-igp.ac.cn

Abstract: The XiLuoDu reservoir dam located on the Jinsha River is one of the largest dams in the world. Nearby faults are very active, and two M>7 strong earthquakes have occurred around the dam. Simulating the rupture dynamics of potential earthquakes on the surrounding faults is very important to estimate the seismic hazard for the dam. In this research, we use the curved grid finite difference method (CG-FDM) to simulate spontaneous ruptures on the major faults around the dam. The main results are that the Leibo middle and south faults (LBMF and LBSF) are more likely to have large destructive earthquakes than the Mabian-Yanjin east fault (MB-YJEF). Asperities on faults that have an impact on strong ground motion are formed under the combined influence of the regional background stress field and fault geometry. Spontaneous ruptures on the LBMF and LBSF are mainly strike-slip with minor thrust components, while those on the MB-YJEF are strike-slip and thrust; these results are consistent with the focal mechanisms of recorded small and moderate earthquakes in this area.

Keywords: Spontaneous rupture dynamics, potential earthquakes, XiLuoDu dam, CG-FDM method

1 Introduction

The Jinsha River, with a total length of 3364 km, is located in the upper reaches of the Yangtze River in China and is rich in water energy resources. There are four world-class reservoir dams on its lower reaches. The XiLuoDu reservoir is located in the Jinsha River gorge section between Leibo County in Sichuan Province and Yongshan County in Yunnan Province; it has a total reservoir capacity of 13.6 billion m^3 and a maximum dam height of 278 m (https://www.ctg.com.cn/sxjt/zt98/cyjsj/xwtqh/313438/index.html). This reservoir is a large-scale project that is useful for power generation, flood control, sediment retention and improvement of downstream shipping conditions, but the reservoir is located within the Daliangshan sub-block at the junction of the Qinghai-Tibetan block and the South China block (Deng et al., 2003; Diao et al., 2014; Zhang et al., 2003). The seismicity and earthquake intensity are both very strong in this area. The seismic resistance of the reservoir dam is very important (https://www.ctg.com.cn/sxjt/zt98/cyjsj/xwtqh/313438/index.html), and a more accurate estimation of earthquake disasters in the dam site area is urgently needed.

Some faults are active around the dam. The Lianfeng fault (LFF) and many small faults in the Mabian-Yanjin fault zone are mainly distributed within 20-30 km of the XiLuoDu dam, forming a nearly triangular small block called the Leibo-Yongshan triangular block. The western boundary of the triangular block is the Ebian-Jinyang fault (EB-JYF), the southern boundary is the Lianfeng fault, and the eastern boundary of the block is composed of three small faults: the Lidian fault (LDF), MaNao fault (MNF), and XieZiBa fault (XZBF) (Figure 1). The EB-JYF, LDF, MNF, and XZBF all belong to the NNW-trending Mabian-Yanjin Fault Zone. These faults are the major seismogenic faults around the dam site and generally show sinistral strike-slip and thrust movements (Wang et al., 2015; Zhao et al., 2014). The tectonic activity and seismicity are very strong around these faults. In particular, two strong earthquakes with M>7.0 have occurred within 50 km of the reservoir dam, including the Mahu M 7.0 earthquake in 1216 and the Daguan M 7.1 earthquake in 1974. Strong earthquakes with M>7 could also possibly occur on the LBMF and LBSF, which are closer to the dam. Therefore, simulating the rupture dynamics of potential strong earthquakes on these faults can help us understand the possible characteristics of earthquake sources more clearly and can provide more accurate ground motions to estimate seismic hazards, which may have great significance for improving the seismic fortification level.

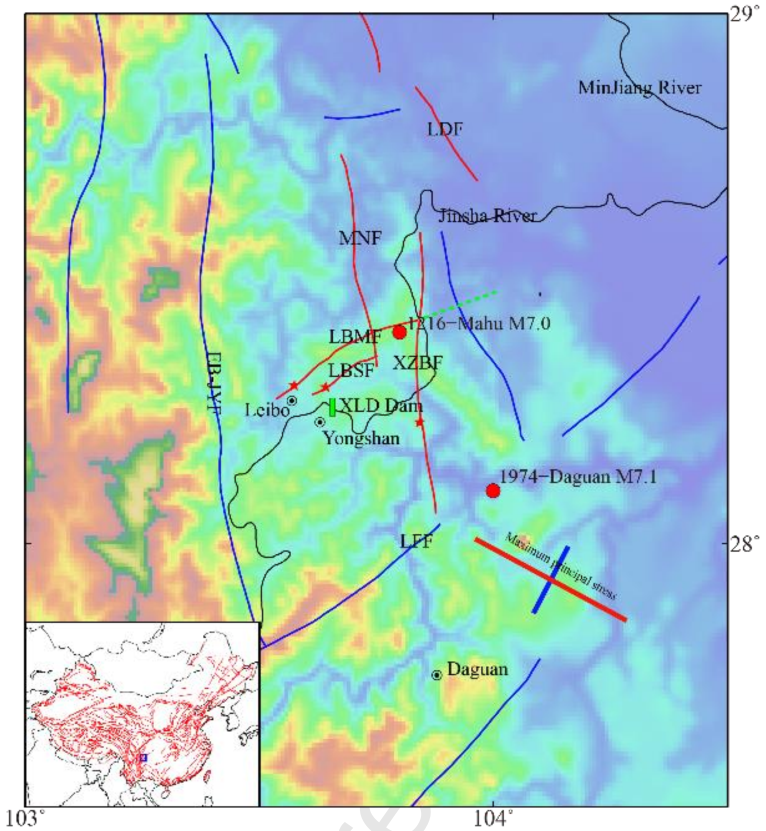

Figure 1. Regional geologic tectonics and stress field. EB-JYF: EBian-JinYang fault; LFF: LianFeng fault; LBMF: LeiBo Middle fault; LBSF: LeiBo South fault, XZBF: XieZiBa fault; MNF: MaNao fault; LDF: LiDian fault; XLD Dam: XiLuoDu Dam. The thick red line represents the maximum principal stress direction, and the thick perpendicular blue line represents the minimum principal stress direction. The simulated target faults (LBMF, LBSF and MB-YJEF) are represented by thin red solid lines. The nucleation zones of the scenario earthquake sources are represented by red stars, and the green dashed line represents the extended segment of the LBMF, which is discussed in section 3.1.2.

2 Method and Model

The rupture process of an earthquake is impacted by several factors, such as the fault geometry, regional stress field, rock properties, surface of the Earth, and site effects. A powerful numerical tool is required to include these complexities in the simulation and derive reliable solutions. We use the curved grid finite difference method (CG-FDM in short) (Zhang et al., 2016; Zhang et al., 2014) to model the spontaneous dynamic rupture of these faults around the XiLuoDu dam. This method has been validated by recent benchmark models (Harris R. A., 2009). Zhang et al., used this method to simulate the potential earthquakes around the Taiyuan Basin in northern China (Zhang et al., 2017) and the Wenchuan M 8.0 earthquake on the Longmenshan fault in China (Zhang et al., 2019).

In this study, the spontaneous rupture processes of potential earthquakes occurring on the faults near the XiLuoDu reservoir dam are simulated by the CG-FDM model, which can reflect the regional three-dimensional velocity structure difference, regional background stress field, and geometry of faults.

2.1 Fault structure

(1) LBMF

The mean strike direction of the LBMF is S63°W, the dip angle is ∠60°, and the length and width of the LBMF are 60 km and 20 km, respectively (Song, 2018, personal communication).

(2) MB-YJEF

Considering that a strong earthquake of magnitude 7 or above could potentially occur in the target area, the three small faults (Lidian, MaNao and Xieziba) are connected into one fault for the simulation, which is called the MaBian-YanJin east fault (MB-YJEF). The mean strike direction of MB-YJEF is S23°E, the dip angle is ∠80°, and the length and width of MB-YJEF are 100 km and 40 km, respectively (Song, 2018, personal communication).

(3) LBSF

The mean strike direction of the LBSF is S59°W, the dip angle is ∠60°, and the length and width of the LBSF are 40 km and 20 km, respectively (Song, 2018, personal communication).

Earthquakes, especially those with large rupture areas, usually begin in a certain area that reaches the rupture conditions and then propagate outwards. To simulate the rupture process of an earthquake, a nucleation zone is also needed. In this zone, the shear stress is artificially set to a value higher than the fault strength, which makes the zone the initial rupture site and then causes the spontaneous rupture of other areas along the fault plane. In this research, the radius of the nucleation zone is set at 3 km. The irregular fault traces, nucleation zones (red stars) and stress directions are also illustrated in Figure 1. Generally, the focal depth of potential earthquakes is set at 12 km in this study.

2.2 Stress state and dynamics parameters

Geological observation data and inversion of the focal mechanism of small and moderate earthquakes in the study area show that the faults are mainly strike-slip faults. The relative magnitude of the triaxial stress of strike-slip earthquakes should be $\sigma_H > \sigma_v > \sigma_h$. Guo (2018) used the focal mechanisms of regional earthquakes and the MSATSI software package (Martínez-Garzón et al., 2014) to obtain the regional stress field (Guo, 2018, personal communication). According to her results, the maximum horizontal principal stress direction is 113°, and the stress shape ratio is $R = \frac{\sigma_V - \sigma_H}{\sigma_h - \sigma_H} = 0.6$ in this area, where σ_H, σ_h, and σ_v are the maximum horizontal principal stress, minimum horizontal principal stress, and vertical principal stress, respectively. These results are consistent with the results of Diao et al. (2014) and Ruan et al. (2010).

When the friction coefficient of the fault is 0.4 and the pore pressure is equal to the hydrostatic pressure, the maximum principal stress σ_H at a depth of 10 km can be taken as 1.7 σ_v, and the minimum principal stress σ_h can be taken as 0.6 σ_v (Zhou, 2014). Therefore, according to this result and the stress shape ratio (R value), the following stress relations are applied in this study:

$$\sigma_v = (\rho - \rho_w)gh,\ \sigma_H = 1.6\sigma_v,\ \sigma_h = 0.6\sigma_v \quad (1)$$

$$\sigma_v = (\rho - \rho_w)gh,\ \sigma_H = 1.45\sigma_v,\ \sigma_h = 0.7\sigma_v \quad (2)$$

$$\sigma_v = (\rho - \rho_w)gh,\ \sigma_H = 1.3\sigma_v,\ \sigma_h = 0.8\sigma_v \quad (3)$$

where ρ and ρ_w are the densities of the overlying rock and water, respectively, h is the depth from a particle to the surface and g is the acceleration of gravity. Generally, the main sliding volume of earthquakes occurring in the Earth's crust is concentrated in the area above 15 km depth; deeper media enter the plastic deformation area, where fewer earthquake events occur. Therefore, the stress is calculated by equations (1-3) within 15 km depth, gradually changing to hydrostatic pressure in the depth range of 15 km – 19 km where the triaxial stresses are equal.

In this paper, the slip weakening law (Ida, 1972) is used as the friction criterion. The critical sliding distance (DC in short) is 0.4 m; when it is less than the critical sliding distance, the static friction coefficient decreases gradually until it reaches the critical sliding distance and then changes to the dynamic friction coefficient; the static friction coefficient μ_s = 0.4, and the dynamic friction coefficient μ_d = 0.25 in this study. According to these parameters, the models are set as shown in Table 1.

Table 1 The parameters of the models used in this research

	Strength of stress	Location of nucleation zone	Set asperity number	The critical sliding distance	Friction coefficient
Model A	Equation (2)	Next to the dam	1	0.4	$\mu_s = 0.4$ $\mu_d = 0.25$
Model B	Equation (3)	Next to the dam	1	0.4	$\mu_s = 0.4$ $\mu_d = 0.25$
Model C	Equation (2)	Far from the dam	1	0.4	$\mu_s = 0.4$ $\mu_d = 0.25$
Model D	Equation (1)	Next to the dam	2	0.4	$\mu_s = 0.4$ $\mu_d = 0.25$

2.3 Velocity structure

The study area is located at the southeastern edge of the Qinghai-Tibetan Plateau, where the boundary marks the collision between the Indian plate and the Eurasian plate and the velocity structure is complex (Wu et al., 2006). The complex velocity structure plays an important role in earthquake rupture and strong ground motion, and a simple velocity model cannot accurately reflect the ground motions and earthquake disasters caused by real earthquakes in the near field. The 3D velocity structure used in our study is inversed from a high-resolution seismic array (ChinArray) by Zheng et al. (2016), which can provide better constraints for the media in the study area.

3 Results

3.1 Simulation on LBMF

3.1.1 The parameters set for Model A

To accurately reflect the rupture process of an earthquake, a 100 m grid is used in our simulations. On this fault, an 10 s spontaneous rupture process is simulated, and snapshots of dislocations are shown in Figure 2. The rupture starts from the nucleation zone (earthquake source) and propagates until it reaches the boundary of the fault. Under the action of the background stress field and fault geometry, an little asperity forms (according to the definition , an asperity is a relatively independent high-stress area on a fault plane before an earthquake (Aki, 1984; Kanamori and Stewart, 1978)) at the southern direction of epicenter (Figure 2c,d). During the earthquake, high-intensity coseismic dislocations occur on the southwestern segment of the fault. The dislocations are not uniform because of the existence of the asperity and the northern geometric turn of fault which stops the rupture at depth. The dislocation at the asperity is the largest. From the rupture time contours (Figure 3), we can see that the rupture accelerates when it reaches the ground surface, which means supershear has occurred, and the small fracture shown in Figure 3 is induced by the artificially set roughness on the fault plane, which is helpful for radiating random high-frequency vibrations. Because the triaxial stresses are equal, the effective shear stress in the deep part of the fault decreases to zero, the sliding gradually stops, and the fault tends to heal before it propagates to the deep boundary of the fault. Therefore, the dislocations are concentrated above 15 km. The rupture propagates on both sides of the fault along the strike direction.

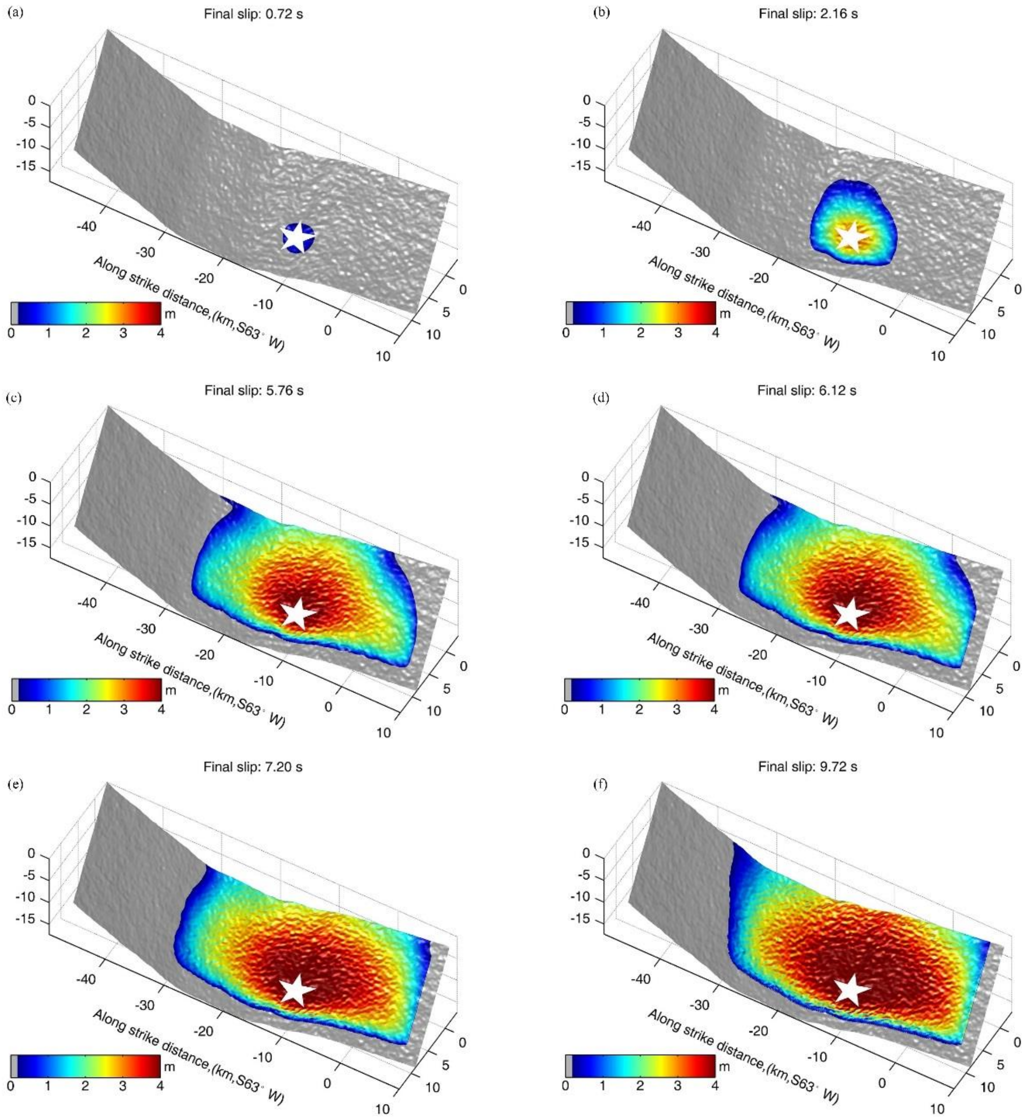

Figure 2. Snapshots of dislocations on the LBMF; the white star represents the hypocenter on each snapshot.

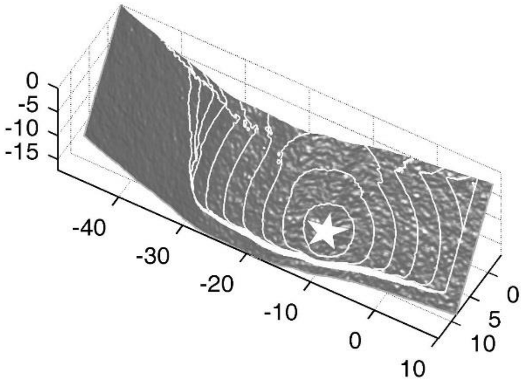

Figure 3. Rupture time contours every 1 s (denoted by white line); the white star represents the hypocenter.

The final slips in the strike and dip directions on the LBMF are shown in Figure 4. The slip is mainly distributed in the strike direction, and the dislocation in the dip direction is small. The figure also shows that the simulated earthquake is a strike-slip earthquake with a minor thrust component, which is consistent with the setting of the background stress field (stress value and stress direction) and focal mechanisms of recorded earthquakes on this fault.

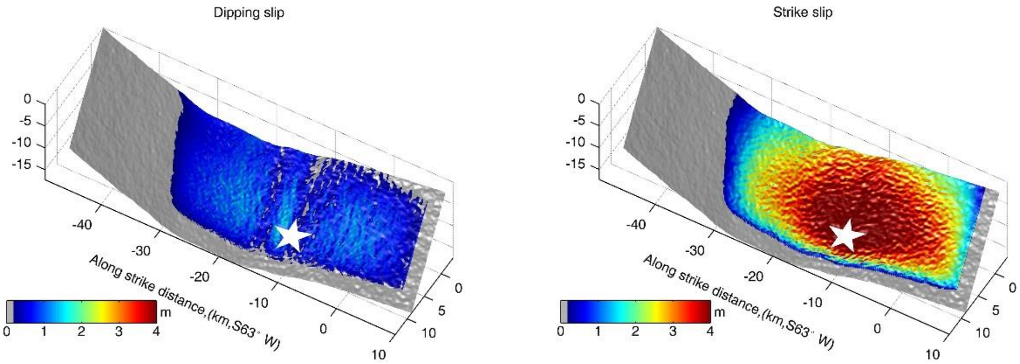

Figure 4. Distribution of the final slips along the dip (left) and strike directions (right); the white stars represent the hypocenter.

The source time function shows that most moment energy is released between 1 and 5 s and that the moment magnitude of this potential earthquake on the LBMF reaches 7.21. A geometric turn in the northeastern segment of the LBMF gradually stops the rupture can be seen in Figure 2 and 4 clearly.

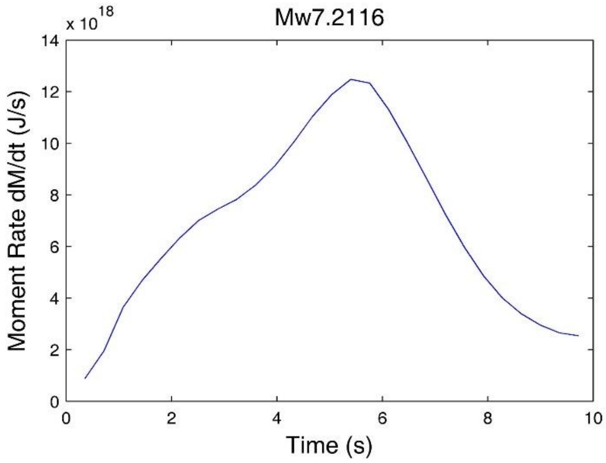

Figure 5. Source time function of the potential earthquake on the LBMF

The rupture is gradually stopped by the geometric turn of the fault, as shown in Figure 2. We would like to know how the rupture propagates when it meets the geometric turn, so we extend the LBMF along the strike direction for 40 km (represented by the green dashed line in Figure 1) to simulate the spontaneous rupture process of the potential earthquake for 8 s under the same background stress field setting. Snapshots of dislocations are shown in Figure 6. Like the rupture on the shorter LBMF, the rupture also starts from the nucleation zone (earthquake source) and an obvious asperity formed in the southern direction of epicenter (Figure 6b). But, unlike the rupture stops in the simulation on the shorter LBMF, a new asperity forms at the geometric turn on the extended LBMF (Figure 6d,e), which helps the rupture continue to propagate; finally, two regions divided by geometric turn on the fault undergo significant slip. The potential earthquake on this longer LBMF also shows that the simulated earthquake is a strike-slip earthquake with a minor thrust component. The moment magnitude of this potential earthquake on the LBMF reaches 7.34, and the seismic moment is accelerated a second time when the rupture propagates to the asperity at the geometric turn which shows completely different fracture characteristics.

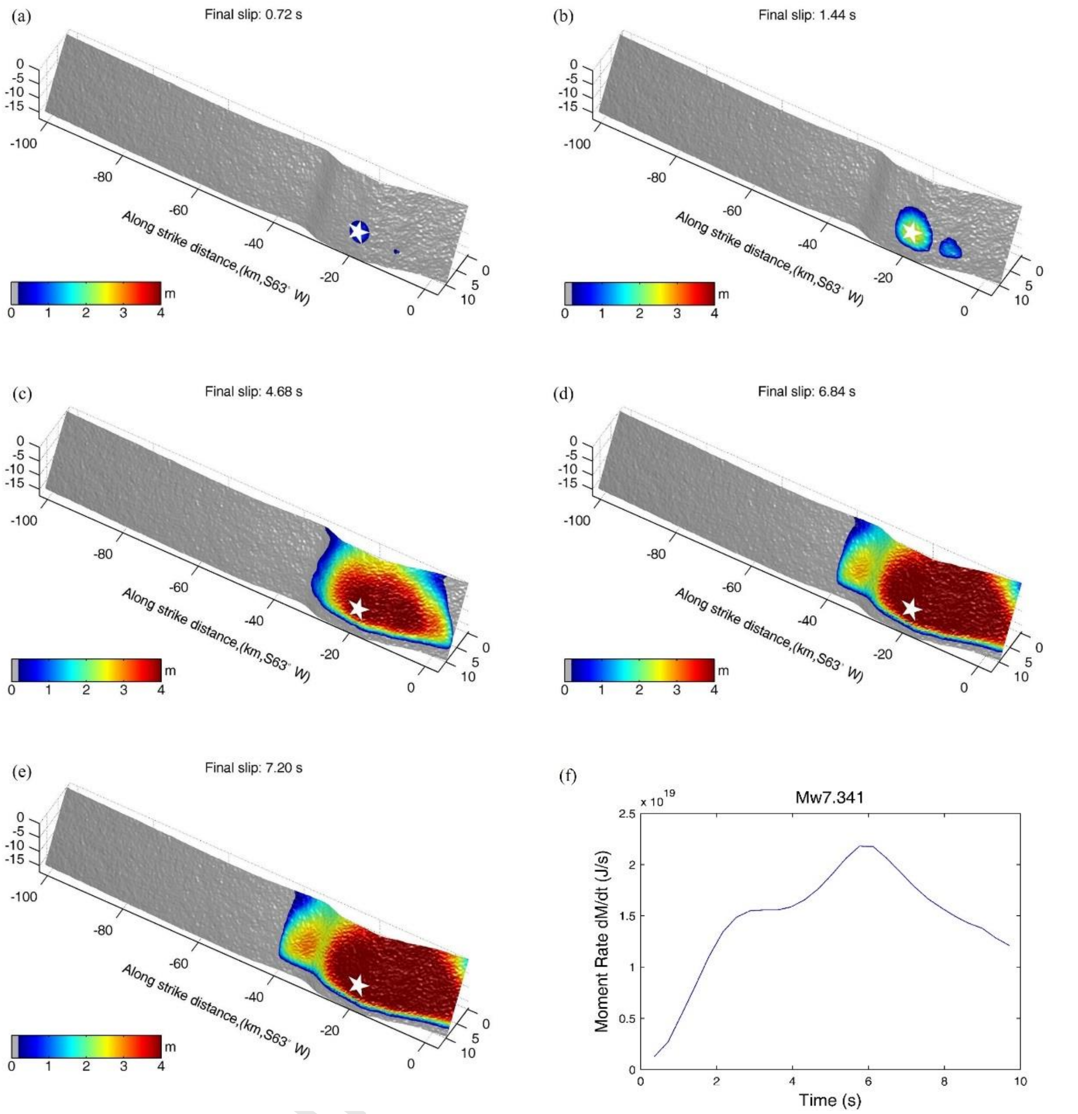

Figure 6. Snapshots of the dislocations and the source time function on the extended LBMF; the white stars represent the hypocenter.

In the simulation of a potential earthquake on the extended LBMF, the dislocations are much less uniform because of the asperity at the geometric turn. The different dislocation distributions and earthquake source time functions can influence the strong ground motion and shaking intensity at the reservoir dam. Therefore, clarifying the fault geometry is also very important for estimating seismic hazards.

3.1.2 The parameters set for Model B

In this setting, the direction and relative size of the background stress field are the same as in the previous section, but the absolute value of the stress field is smaller than that in the previous section. The final slip is distributed only at the nucleation zone, and the source time function shows that the spontaneous rupture stops gradually after 2 s and that the rupture cannot spread along the fault plane (Figure 7).

This event fails to develop into a more destructive earthquake (Xu et al., 2015).

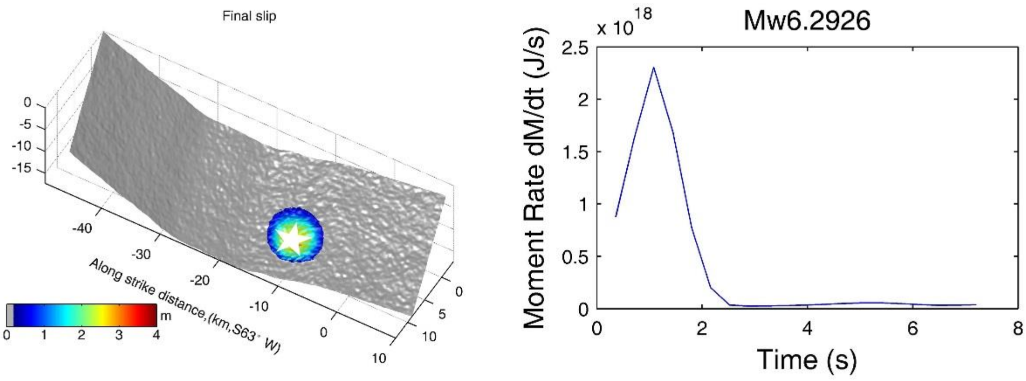

Figure 7. The final dislocation and the source time function on the LBMF under smaller stress (model B); the white star represents the hypocenter.

3.1.3 The parameters set for Model C

As we can see, the nucleation zone of the model is set next to the dam site, and there is random roughness on the fault plane in section 3.1.1 and section 3.1.2. In this section, a simulation is run on a smooth fault plane with a nucleation zone far from the dam site to see the rupture process. From the time process of the rupture (Figure 8a), it can be seen that the rupture starts from the nucleation zone and propagates toward both sides and the shallow part of the fault. In the deep part of the fault, the rupture propagates to both sides with difficulty due to the blockage by the geometric turn of the fault. Unlike the rupture time in Figure 3, there is no microfracture on the smooth fault plane in Figure 8a. The final slip on the fault plane also illustrates that the rupture cannot propagate because of the geometric turn of the fault (Figure 8b). The source time function shows the seismic energy released during 0-3 s, and the moment magnitude only reaches 6.5. The seismic moment is accelerated a second time during 4-6 s when the rupture touches ground surface. The simulated result reveals that the magnitude of a potential earthquake is much smaller when the nucleation zone is located far from the dam site, and the seismic hazard should be less.

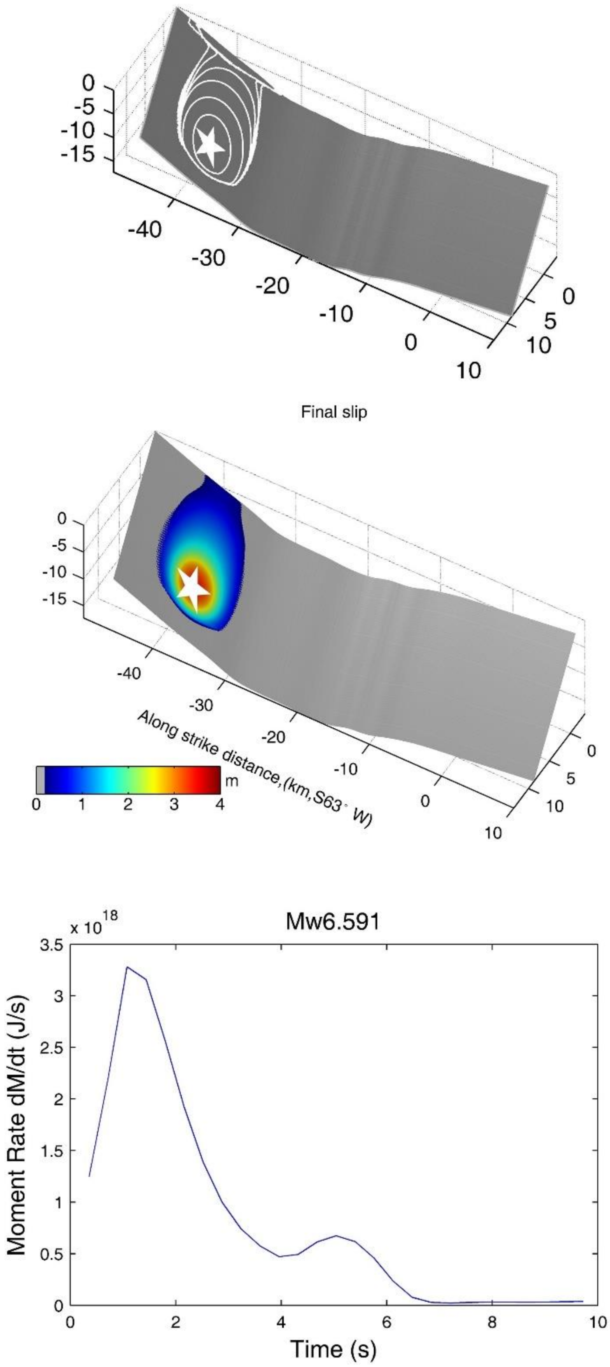

Figure 8. Rupture time contours every 1 s (denoted by white lines, top panel), the final slip distribution (middle panel) and the source time function (bottom panel) of a potential earthquake induced by a nucleation zone far from the dam site on a smooth fault plane for the LBMF. The white star represents the hypocenter.

3.2 Simulation on the LBSF

3.2.1 The parameters set for Model A

The strike direction of the LBSF is similar to that of the LBMF, but the LBSF is shorter. In the spontaneous rupture, two asperities form on the north side of the nucleation zone. The rupture starts from the asperity and nucleation zone and then gradually expands to produce an Mw 7.16 earthquake (Figure 9). As mentioned above, we set the shear stress higher than the fault strength in the nucleation zone to make the rupture expand from here. In Figure 9, we can see that there is one location (located in the northeastern segments of the LBSF) slide prior to the propagation of rupture, and the dislocation of this region is remarkable. This shows that this location slide more easily, and we speculate that the background stress fields at this location is larger due to the fault geometry there. Therefore, if a real destructive earthquake occurs on the LBSF, these this place is more likely to be the initial fracture point.

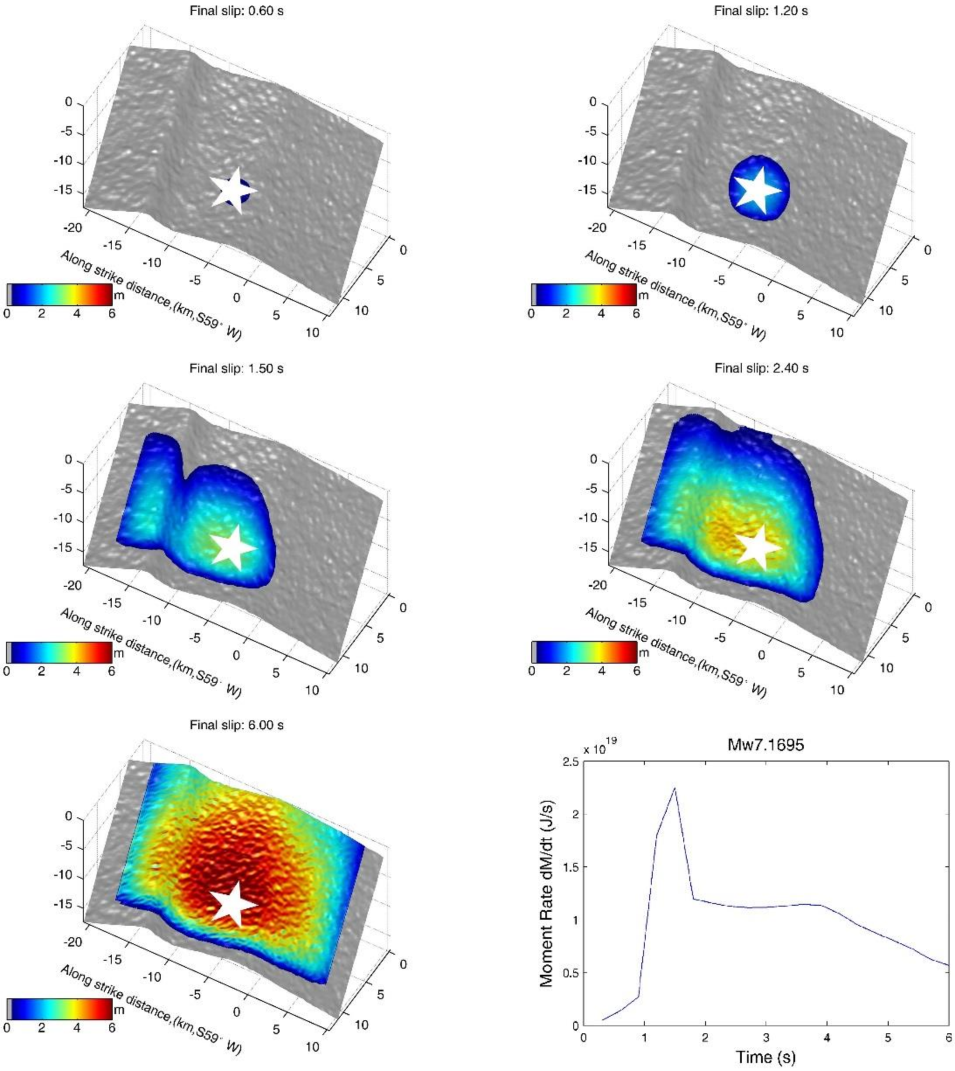

Figure 9. Snapshots of the dislocations and the source time function on the LBSF; the white stars represent the hypocenter.

3.2.2 The parameters set for Model B

Under this setting, the spontaneous rupture is similar to the simulated result on the LBMF in section 3.1.2; the spontaneous rupture stops gradually after 2 s, and the rupture cannot propagate. It fails to develop a more destructive earthquake.

3.3 Simulation on MB-YJEF

3.3.1 The parameters set for Model A

In this simulation, the magnitude and direction of the stress field remain the same as the setting used in the simulations on the LBMF and LBSF in sections 3.1.1and 3.2.1. From the final slip and source time function, the results are the same as the results in section 3.1.2: spontaneous rupture stops gradually after 2 s, and the rupture cannot propagate (Figure 10). It fails to develop a more destructive earthquake under this setting of the stress field.

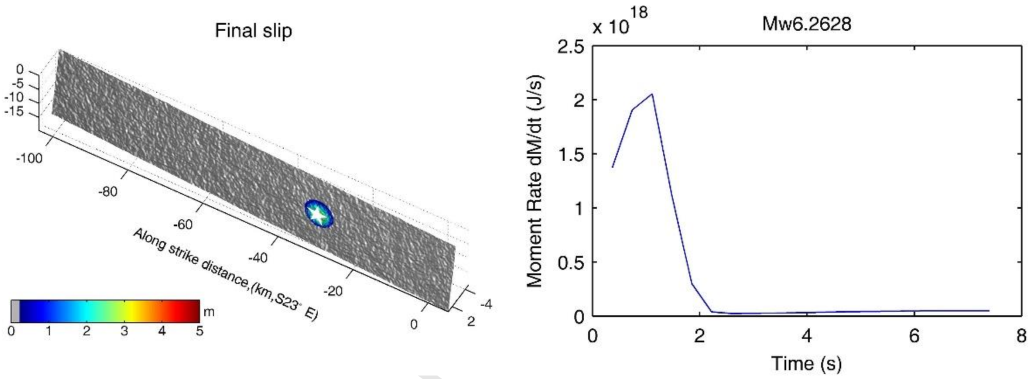

Figure 10. The final dislocation and the source time function on the MB-YJEF; the white star represents the hypocenter.

3.3.2 The parameters set for Model D

To simulate the spontaneous rupture process on the MB-YJEF, the background stress field should be set larger with $\sigma_H = 1.6\sigma_v$ and $\sigma_h = 0.6\sigma_v$. Under this setting, the rupture starts from the nucleation area and expands along both sides of the fault until reaching the boundary of the fault. A rectangular asperity of approximately 80 km^2 is set north of the earthquake source (located almost in the middle of the MB-YJEF) following the self-similar empirical formula for the asperity size derived by Somerville et al. (1999), which can be seen clearly in Figure 11. There are two regions with large dislocations (denoted by black rectangle): one is located in the nucleation zone, and the other forms in the area with the asperity. The distribution of dislocations is inhomogeneous, which may be induced by the existence of the asperity. From the snapshots of slip rate in the strike direction, we can see that supershear occurs on the fault, although the rupture does not reach the surface during 2.4 s -2.7 s (Figure 12b, c). Generally, supershear occurs after the fracture of a strike-slip earthquake touches the surface because the stress loading caused by SV-P wave conversion at the surface can induce supershear fracture (Xu, 2014). However, when the initial background stress (σ_0) is high, S in the formula $S = \frac{\sigma_p - \sigma_0}{\sigma_0 - \sigma_d}$ meets the condition of a value less than 1.7, and supershear fracture also occurs (Andrews, 1976; Das and Aki, 1977), which is shown in this simulation (Figure 12b,c).

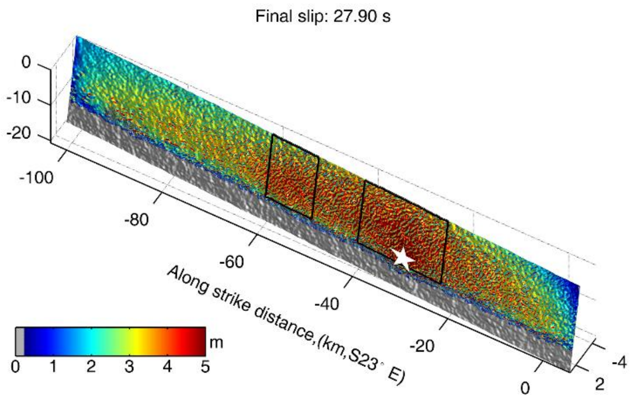

Figure 11. The final slip on the MB-YJEF surface. The white star represents the hypocenter, and the black circles depict two areas with large dislocations.

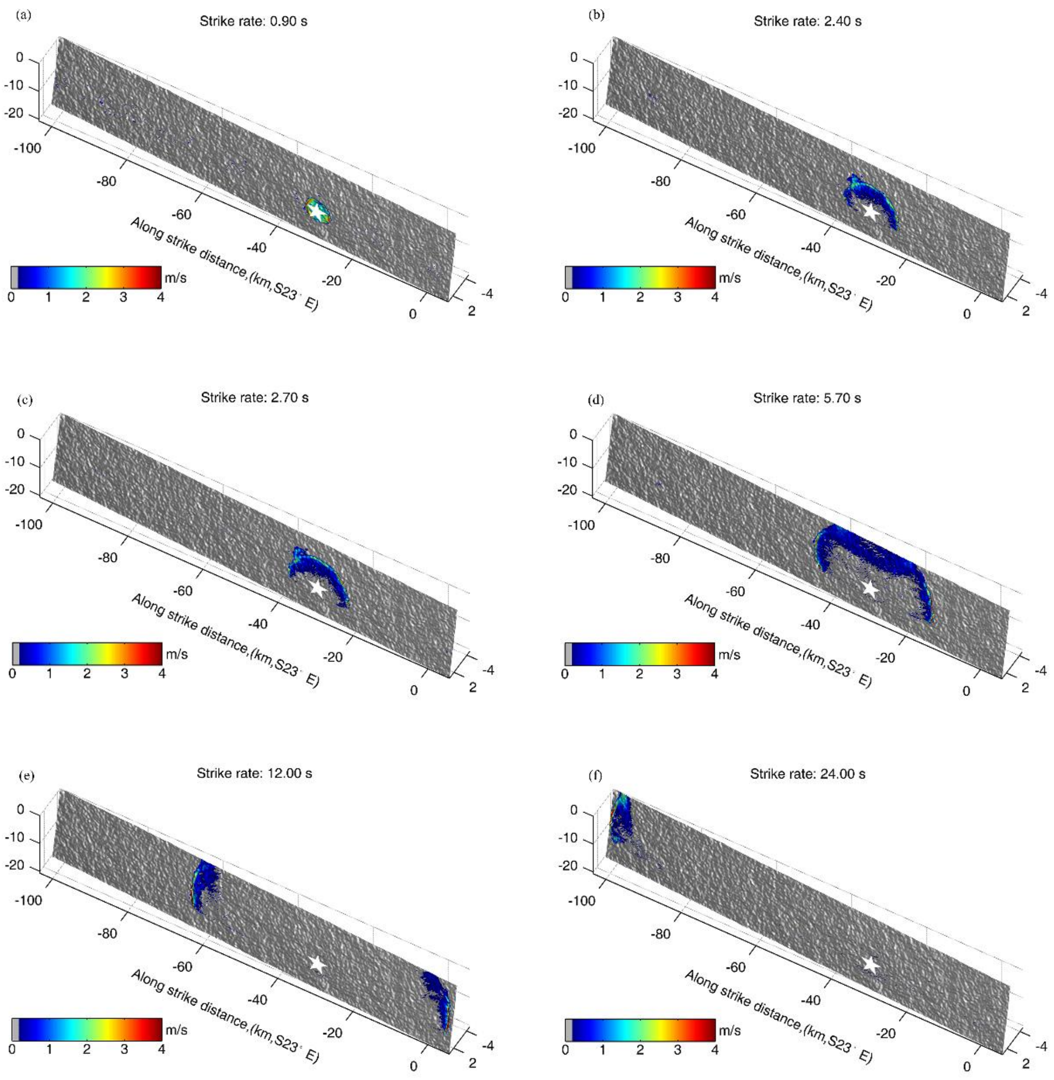

Figure 12. Snapshots of the strike-slip component of the slip rate along the MB-YJEF surface. The white stars represent the hypocenter for each snapshot.

The final slips in the strike and dip directions on the MB-YJEF are shown in Figure 13. The slips are distributed almost evenly along the strike and dip directions on the fault plane, which is consistent with the inversed results of earthquake mechanisms: strike-slip and thrust motions (Guo, 2018, personal communication). The dislocations at the region with the asperity increase obviously, and the seismic moment magnitude can reach 7.5 in a 35 s earthquake rupture process. When the rupture slides to the asperity, the seismic moment is released again. The small amount of seismic moment release during 28-34s maybe induced by the boundary effect, and finally stop after 34s.

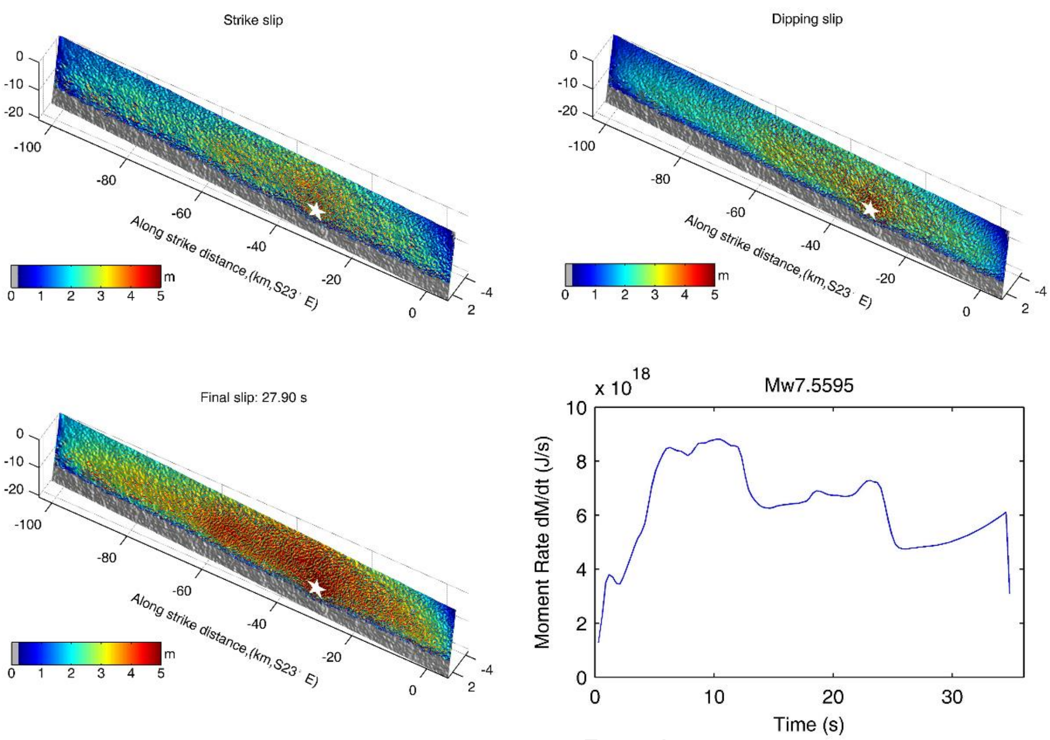

Figure 13. The slips along the strike and dip directions (top panel). The final slip on the MB-YJEF and the earthquake source time function (bottom panel). The white stars represent the hypocenter.

In summary, compared with the simulated results for the spontaneous ruptures of the MB-YJEF, LBMF, and LBSF, a higher background stress is needed to trigger a strong earthquake with magnitude >7 on the MB-YJEF; that is, under the same regional background stress field, the LBMF and LBSF slip more easily and generate stronger earthquakes.

4 Discussion

4.1 Regional stress field

The dominant direction of the horizontal principal compressive stress axis of the modern tectonic stress field in this region is NWW(Cheng, 1981; Cui et al., 2006), and the movement of the block is also in this direction(Zhang et al., 2004), which indicates that the regional stress is mainly strike-slip. The maximum horizontal principal stress direction determined in our model is 113°, and the rupture processes on the LBMF and LBSF show that the earthquakes are mainly strike-slip. The strike direction of the MB-YJEF is 157°, and its intersection angle with the maximum horizontal principal stress direction is almost 45°, which indicates that the rupture process should have thrust components. The simulation results for the MB-YJEF also confirm this feature.

For the magnitude of stress, the relative magnitudes of the triaxial stresses for a strike-slip earthquake should be $\sigma_H > \sigma_v > \sigma_h$, σ_H should be smaller than $1.7\sigma_v$, and σ_h should be larger than $0.6\sigma_v$ (Zhou, 2014). To match these stress shape ratios, the magnitudes of triaxial stress are set according to equations (1-3) in section 2.2.

The aim of this research is to provide more realistic rupture dynamics for estimating the seismic hazard induced by potential earthquakes on seismogenic faults, so we only consider the earthquake source that is closest to the dam site. Under this situation, the nucleation zones of potential earthquakes are set as shown in Figure 1. The stress ratio distribution (calculated by the geometric mean of the shear stress divided by the normal stress) is shown in Figure 14. The nucleation zone and the asperity can be seen clearly. The top panel shows the nucleation zone next to the XiLuoDu dam, and the unevenly distributed high values in Figure 14a are caused by the roughnesses of the faults, which are artificially set. The nucleation zone is far from the dam on a smooth fault (corresponding to the simulation in section 3.1.3) and is shown in the middle panel. The bottom panel shows the fault, which has another asperity in addition to the nucleation zone (corresponding to the simulation in section 3.3.2). The value of the stress ratio is lower in the area with the asperity because a higher shear stress drop occurs.

On the other hand, the fault geometry and background stress field are both major factors that form asperities on faults. The artificially set asperities in Table 1 are only created by the higher initial background stress; however, the asperities in sections 3.1.1 and 3.2.1 are formed by the fault geometries, which make the shear stress higher there.

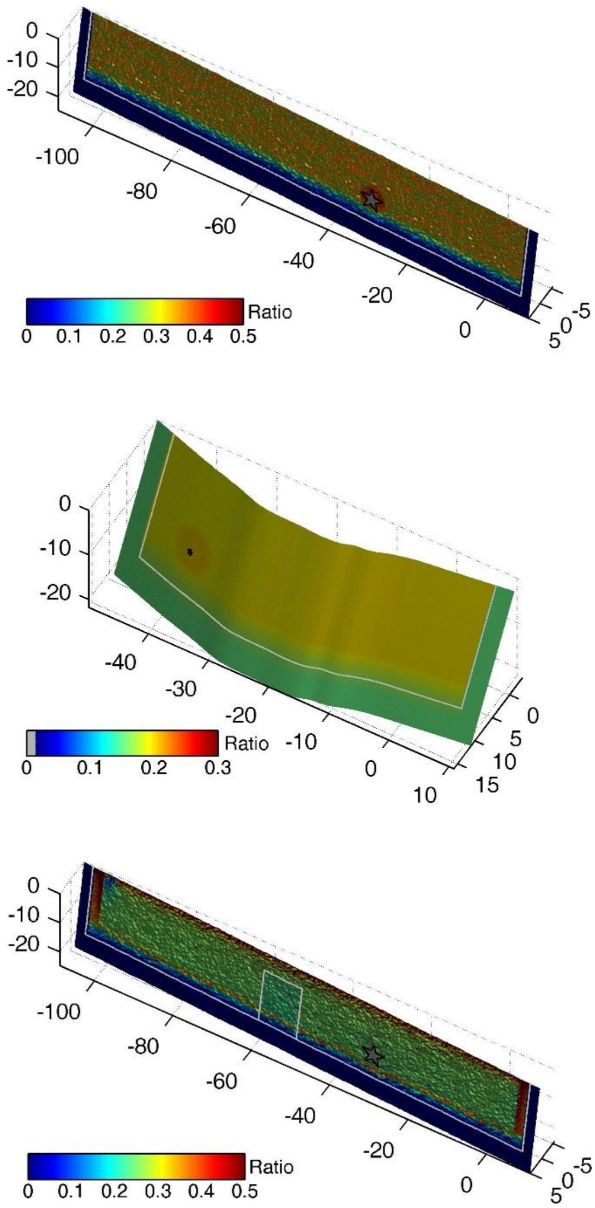

Figure 14. The nucleation zone next to the XiLuoDu dam is shown in the top panel, and the nucleation zone far from the XiLuoDu dam is shown in the middle panel. Another asperity in addition to the nucleation zone is shown in the bottom panel. The gray stars represent the hypocenter. The white lines sketch the allowed rupture area on the fault and the asperity in the bottom panel of the figure.

4.2 Faults in our Model

The Leibo fault zone consists of three parallel NEE-trending faults. It is composed of the north branch fault, middle branch fault and south branch fault from north to south(Han et al., 2009), among which the Leibo middle fault is longest. The Mahu earthquake occurred on the eastern segment of the Leibo middle fault (Han et al.,

2009. Figure 2). The three-dimensional (3D) geometry of the LBMF and LBSF used to model the dynamic rupture are constructed by the surface trace, which is derived from Song (2018, personal communication) and consistent with Han's geological survey, and then are extended at depth as a dipping fault with an angle of 60°.

The Mabian-Yanjin East fault consists of a series of faults, such as XiZiBa (XZBF), LiDian (LDF), and MaNao (MNF)(Han, 1993). The strike direction of these faults is NNW; although the surface traces of these faults are not consistent, they belong to the same basement fault (Han, 1993). At present, we can only simulate the rupture dynamics on a single fault, and cascading ruptures cannot be achieved. Therefore, the MB-YJEF used in our research is digitized by two endpoints along the strike direction to contain the XZBF, LDF and MNF and then extended at depth as a dipping fault with an angle of 80°; as we can see (in section 3.3), this fault is a straight plane fault.

5 Conclusions

In this research, we construct a curved grid finite difference method (CG-FDM) model that includes the 3D velocity, regional stress field, fault geometry and tomography to simulate the rupture dynamics of potential earthquakes on the LBMF, LBSF and MB-YJEF. The results can be summarized as follows:

(1) The background stress field plays a very important role in determining whether the rupture can propagate to develop a destructive earthquake. The fault geometry has a great influence on the rupture pattern of the earthquake.

(2) Under the same regional stress field (stress value and direction), stronger destructive earthquakes are more likely to occur on the LBMF and LBSF than on the MB-YJEF. In particular, the initial rupture is more likely to occur on the side away from the dam on the LBSF.

(3) The final slips are mainly strike-slip with minor thrust components on the LBMF and LBSF; however, the final slips on the MB-YJEF are strike-slip and thrust under a regional stress field. These results are also consistent with regional earthquake mechanisms. When a strike-slip earthquake touches the surface, it develops into a supershear fracture. In the simulation of spontaneous fracture on the MB-YJEF (in section 3.3.2), supershear fracture also occurs when the background stress is high, although the rupture does not touch the surface. Whether a supershear fracture occurs or does not occur produces different effects

on the strong ground motion at the dam site.

(4) The fault geometry and background stress field are the major factors that form asperities on the faults. Asperities play an important role in the final slip of an earthquake, and the slip is larger where asperities exist. In section 3.3.2, we set an asperity on the north side of the earthquake source on the MB-YJEF, which produces two locations with large dislocations. In section 3.1.1, for the LBMF, if the fault length is longer, it is easy to form asperities at the geometric turn of the fault. The existence of asperities has an impact on the strong ground motion at the dam site. Therefore, to clarify the fault geometry, it is also very important to estimate seismic hazards such as the background stress field.

Declaration of Competing Interest

The authors declare that they have no known competing financial interests or personal relationships that could have appeared to influence the work reported in this paper.

Acknowledgments

This work was supported by the National Key Research and Development Program of China (2017YFC0404901), the Special Fund of the Institute of Geophysics, China Earthquake Administration (Grant Number: DQJB19B27) and the National Science Foundation of China (41674105).

References

Aki, K., 1984. Asperities, barriers, characteristic earthquakes and strong motion prediction. Journal of Geophysical Research Solid Earth 89, 5867-5872.

Andrews, D.J., 1976. Rupture velocity of plane strain shear cracks. Journal of Geophysical Research 81, 5679-5687.

Cheng, e., 1981. Recent tectonic stress field and tectonic movement of the sichuan province and its vicinity. Acta Seismologica Sinica 3, 231-241(In Chinese)

Cui, X., Xie, F., Zhang, H., 2006. Recent tectonic stress field zoning in Sichuan-Yunnan region and its dynamic interest. Acta Seismologica Sinica 28, 451-461(In Chinese).

Das, S., Aki, K., 1977. A numerical study of two-dimensional spontaneous rupture propagation. 50, 643-668.

Deng, Q., Zhang, P., Ran, Y., Xiaoping;, Y., Min, W., Lichun, C., 2003. Active tectnoics and earthquake activities in China. Geoscience Frontiers 10, 66-73 (In Chinese).

Diao, G., Wang, R., Feng, X., Wang, X., Feng, Z., Zhang, H., Cheng, W., Li, Y., Wang, L., 2014. Analysis of characteristics of focal mechanism in reservoir region of XILUODU reservoir after impoundment. Seismology and Geology 36, 644-657 (In Chinese).

Han, D., 1993. The tectonic pattern and seismic characteristic of Mabian-Yongshan seismic zone.

Seismology & Geology 15, 253-260.
Han, Z., He, Y., An, Y., Li, C., 2009. A New Seismotectonic Belt :Features of the Latest Structural Deformation Style in the Mabian Seismotectonic Zone. ACTA GEOLOGICA SINICA 83, 218-229.
Harris R. A., B.M., Archuleta R., Dunham E., Aagaard B., Ampuero J. P., Bhat H., Cruz-Atienza V., Dalguer L., Dawson P., Day S., Duan B., ELy G., Kaneko Y., Kase Y., Lapusta N., Liu Y., Ma S., Oglesby D., Olsen K., Pitarka A., Song S., Templeton E., 2009. The SCEC/USGS Dynamic Earthquake Rupture Code Verification Exercise. Seismological Research Letters 80, 119-126.
Ida, Y., 1972. Cohesive Force across the Tip of a Longitudinal-Shear Crack and Griffith's Specific Surface Energy. Journal of Geophysical Research 77, 3796-3805.
Kanamori, H., Stewart, G.S., 1978. Seismological aspects of the Guatemala Earthquake of February 4, 1976. Journal of Geophysical Research Solid Earth 83, 3427-3434.
Martínez-Garzón, P., Kwiatek, G., Michèle, I., Bohnhoff, M., 2014. MSATSI: A MATLAB Package for Stress Inversion Combining Solid Classic Methodology, a New Simplified User‐ Handling, and a Visualization Tool. Seismological Research Letters 85, 896-904.
Ruan, X., Cheng, W.Z., Qiao, H.Z., Zhang, Z.W., Ying, F.U., 2010. Research of Source Parameter and Stress State of Mabian-Daguan Tectonic Zone. Journal of Seismological Research 33, 294-300 (In Chinese).
Somerville, P., Irikura, K., Graves, R., Sawada, S., Wald, D., Abrahamson, N., Iwasaki, Y., Kagawa, T., Smith, N., Kowada, A., 1999. Characterizing crustal earthquake slip models for the prediction of strong motion. Seismological Research Letters 70, 59-80.
Wang, X.S., LJian, Xie, Z.J., Long, F., Zhao, X.Y., Zheng, Y., 2015. Focal mechanisms and tectonic stress field in the North-South Seismic Belt of China. Chinese Journal of Geophysics 58, 4149-4162 (In Chinese).
Wu, J., Ming, Y., Wang, C., 2006. Regional waveform inversion for crustal and upper mantle velocity structure below Chuandian region. Chinese Journal of Geophysics 49, 1369-1376 (In Chinese).
Xu, J., 2014. Study on supershear rupture and ground motion with free surface. University of Science and Techology of China, Hefei, China.
Xu, J., Zhang, H., Chen, X., 2015. Rupture phase diagrams for a planar fault in 3-D full-space and half-space. Geophysical Journal International 202, 2194-2206.
Zhang, P., Deng, Q., Zhang, G., Ma, J., Gan, W., Min, W., Mao, F., Wang, Q., 2003. Strong earthquake activities and active blocks in mainland China. SCIENTIA SINICA Terrae 33, 12-20 (In Chinese).
Zhang, P., Shen, Z., Wang, M., Gan, W., Burgmann, R., Molnar, P., Wang, Q., Niu, Z., Sun, J., Wu, J., Sun, H., You, X., 2004. Continuous deformation of the Tibetan Plateau from global positioning system data. Geology 32, 809-812.
Zhang, Z., Huang, H., Wei, Z., Chen, X., 2016. On the Free-Surface Problem in Dynamic-Rupture Simulation of a Nonplanar Fault. Bulletin of the Seismological Society of America 106, 1162-1175.
Zhang, Z., Zhang, W., Chen, X., 2014. Three-dimensional curved grid finite-difference modelling for non-planar rupture dynamics. Geophysical Journal International 199, 860-879.
Zhang, Z., Zhang, W., Chen, X., 2019. Dynamic rupture simulations of the 2008 Mw 7.9 Wenchuan earthquake by the curved grid finite‐ difference method. Journal of Geophysical Research: Solid Earth.
Zhang, Z., Zhang, W., Chen, X., Li, P.E., Fu, C., 2017. Rupture Dynamics and Ground Motion from Potential Earthquakes around Taiyuan, China. Bulletin of the Seismological Society of America 107, 1201-1212.
Zhao, J., Liu, J., Niu, A.F., Yan, W., 2014. Study on fault locking characteristic around the Daliangshan

sub-block. Seismology & Geology 36, 1135-1144 (In Chinese).

Zheng, C., Ding, Z.F., Song, X.D., 2016. Joint inversion of surface wave dispersion and receiver functions for crustal and uppermost mantle structure in Southeast Tibetan Plateau. Chinese Journal of Geophysics 59, 3223-3236 (In Chinese).

Zhou, C., 2014. The Stress field changes near the bounary fault zones in the Bayanhar Block and their effect on the large earthquakes. PhD Thesis, Chinese Academy of Geological Sciences (In Chinese).

Liao Li: Conceptualization, Methodology, Software, Visualization, Investigation, Data curation, Writing- Original draft preparation, Writing- Reviewing and Editing.

Li Pingen: Conceptualization, Writing- Reviewing and Editing.

Yang Jiansi: Supervision, Writing- Reviewing and Editing.

Feng Jianzhou: Visualization.

Declaration of Competing Interest

The authors declare that they have no known competing financial interests or personal relationships that could have appeared to influence the work reported in this paper.

Highlights.

- Rupture dynamics from potential earthquakes on three major seismogenic faults have been simulated.
- The background stress field and fault geometry play a very important role to decide the rupture dynamics of scenario earthquakes.
- These three faults all have the ability to occur a M >7 earthquake, but the stronger destructive earthquakes are more likely occurred on LBMF and LBSF than that on MB-YJEF

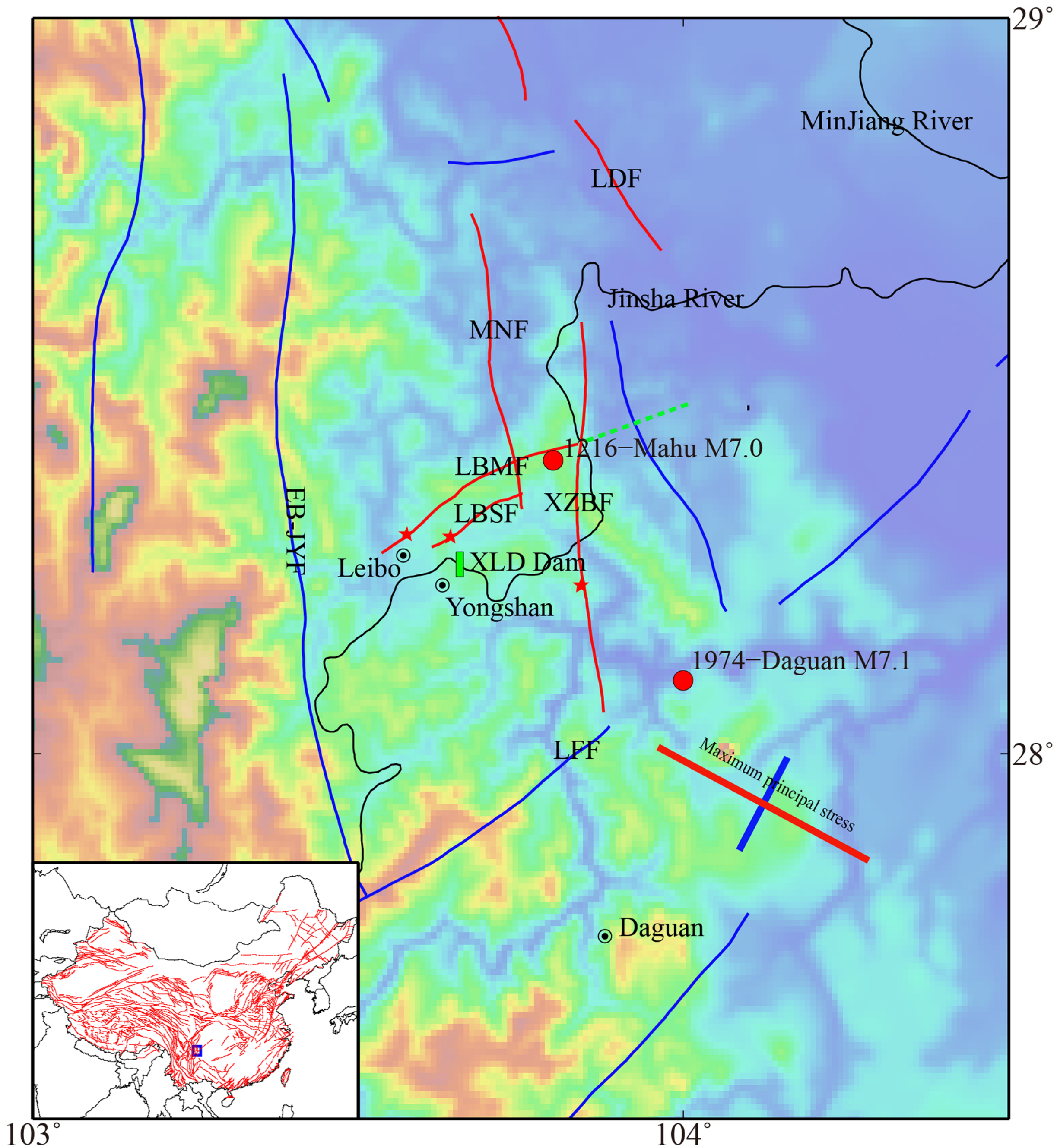
29°
MinJiang River
LDF
Jinsha River
MNF
1216−Mahu M7.0
LBMF
XZBF
LBSF
EB-JYF
Leibo
XLD Dam
Yongshan
1974−Daguan M7.1
LFF
Maximum principal stress
28°
Daguan
103°
104°

Figure 1

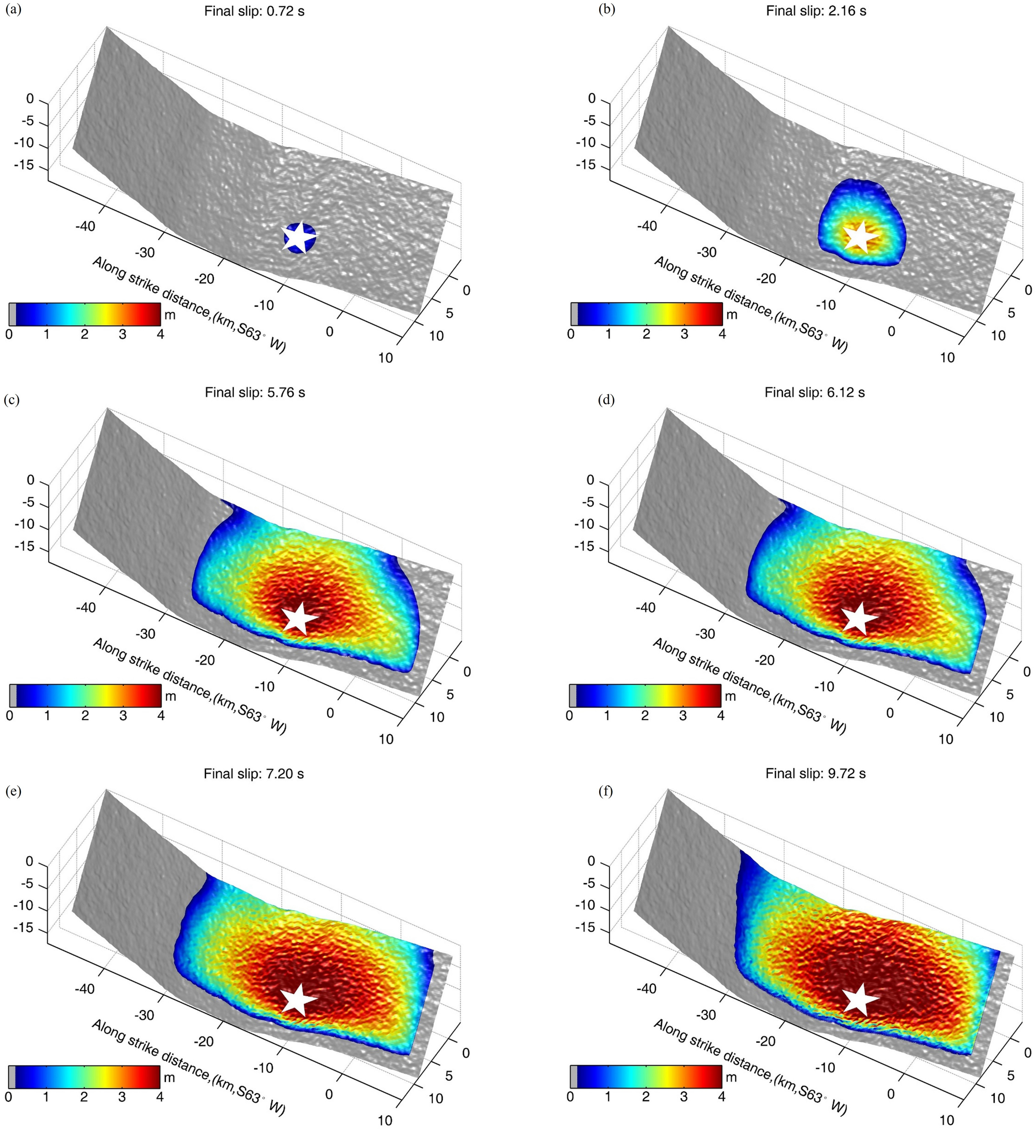

(a)
Final slip: 0.72 s
(b)
Final slip: 2.16 s
(c)
Final slip: 5.76 s
(d)
Final slip: 6.12 s
(e)
Final slip: 7.20 s
(f)
Final slip: 9.72 s
0
-5
-10
-15
-40
-30
-20
-10
0
10
0
5
10
Along strike distance,(km,S63° W)
m
0
1
2
3
4

Figure 2

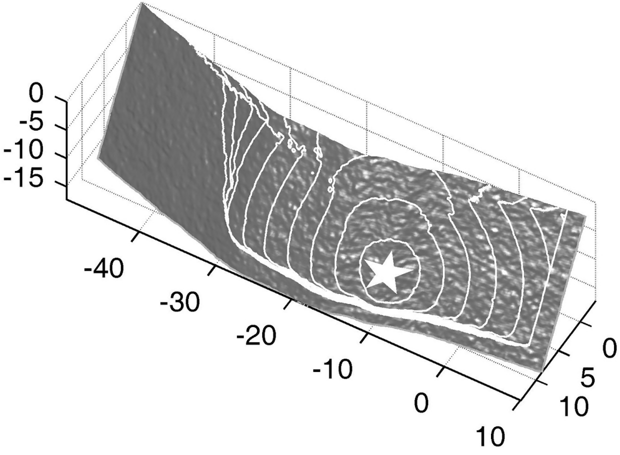

Figure 3

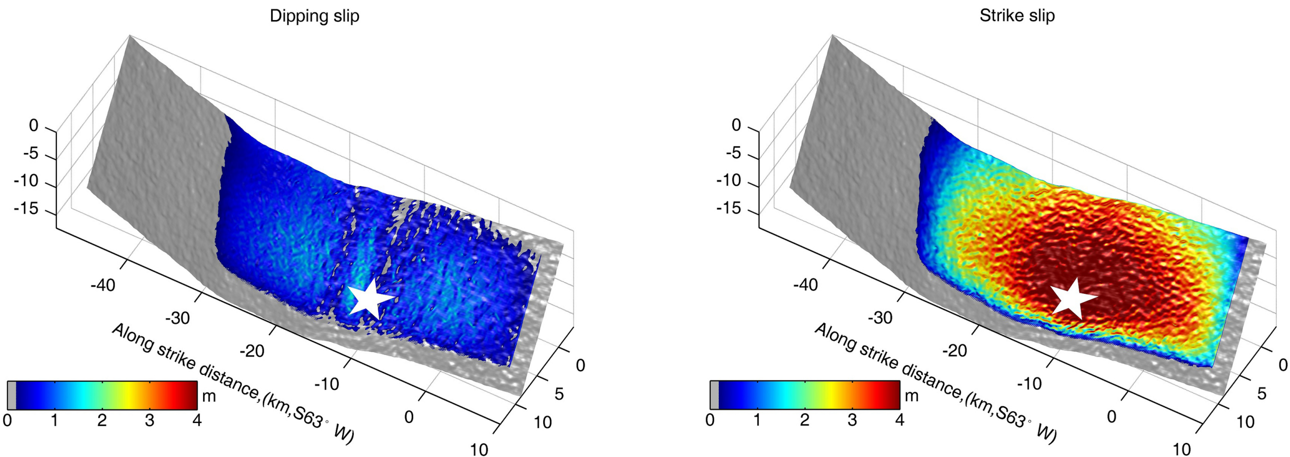
Dipping slip
Strike slip
0
-5
-10
-15
-40
-30
-20
-10
0
10
0
5
10
Along strike distance,(km,S63° W)
m
0
1
2
3
4

Figure 4

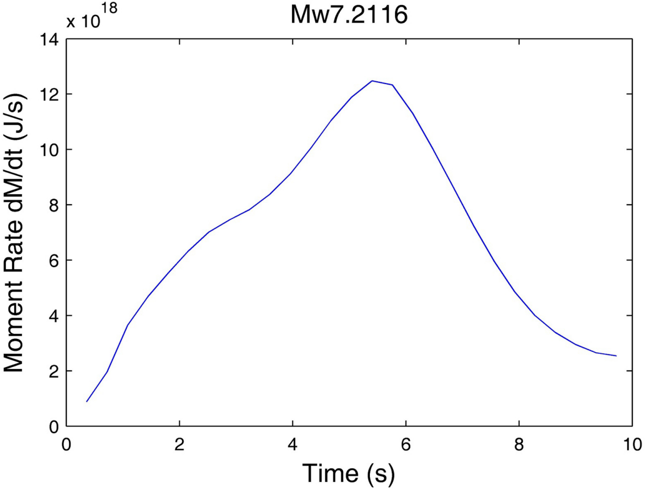

Figure 5

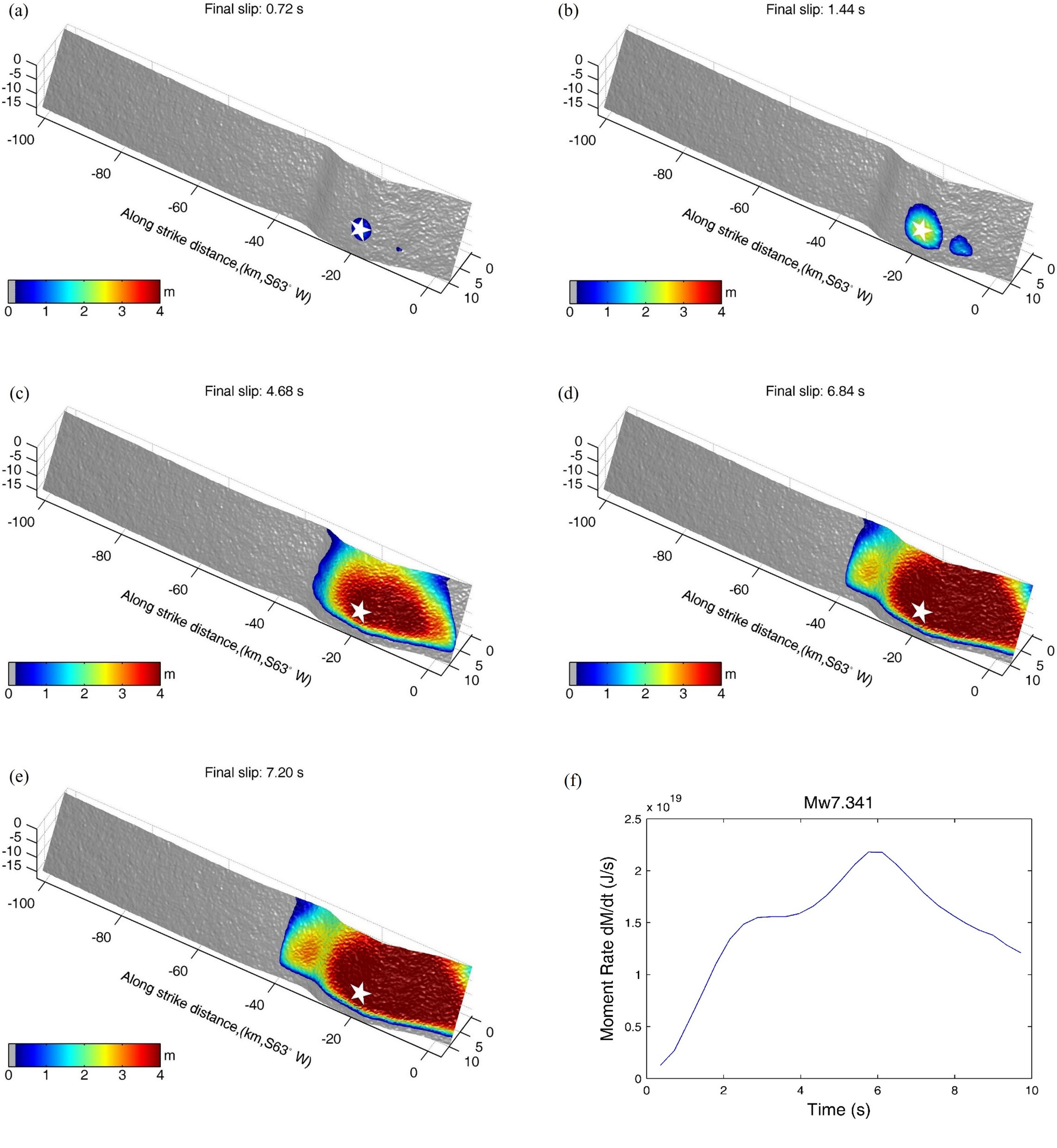

(a)
Final slip: 0.72 s
(b)
Final slip: 1.44 s
(c)
Final slip: 4.68 s
(d)
Final slip: 6.84 s
(e)
Final slip: 7.20 s
Along strike distance,(km,S63° W)
m
0 1 2 3 4
(f)
Mw7.341
x 10^19
Moment Rate dM/dt (J/s)
Time (s)

Figure 6

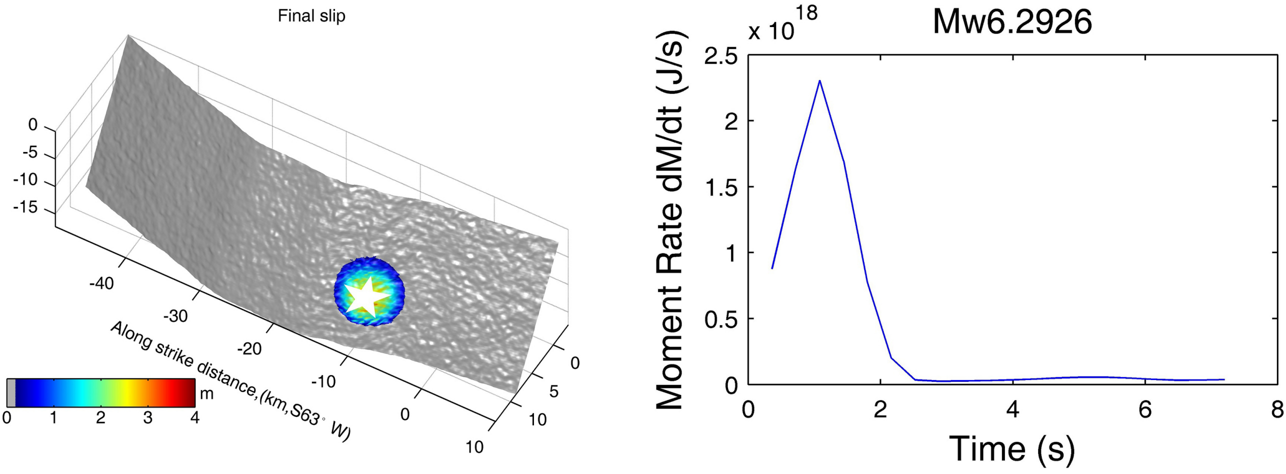

Final slip
0
-5
-10
-15
-40
-30
-20
-10
0
10
Along strike distance,(km,S63° W)
0
5
10
m
0
1
2
3
4
Mw6.2926
x 10^18
Moment Rate dM/dt (J/s)
2.5
2
1.5
1
0.5
0
0
2
4
6
8
Time (s)

Figure 7

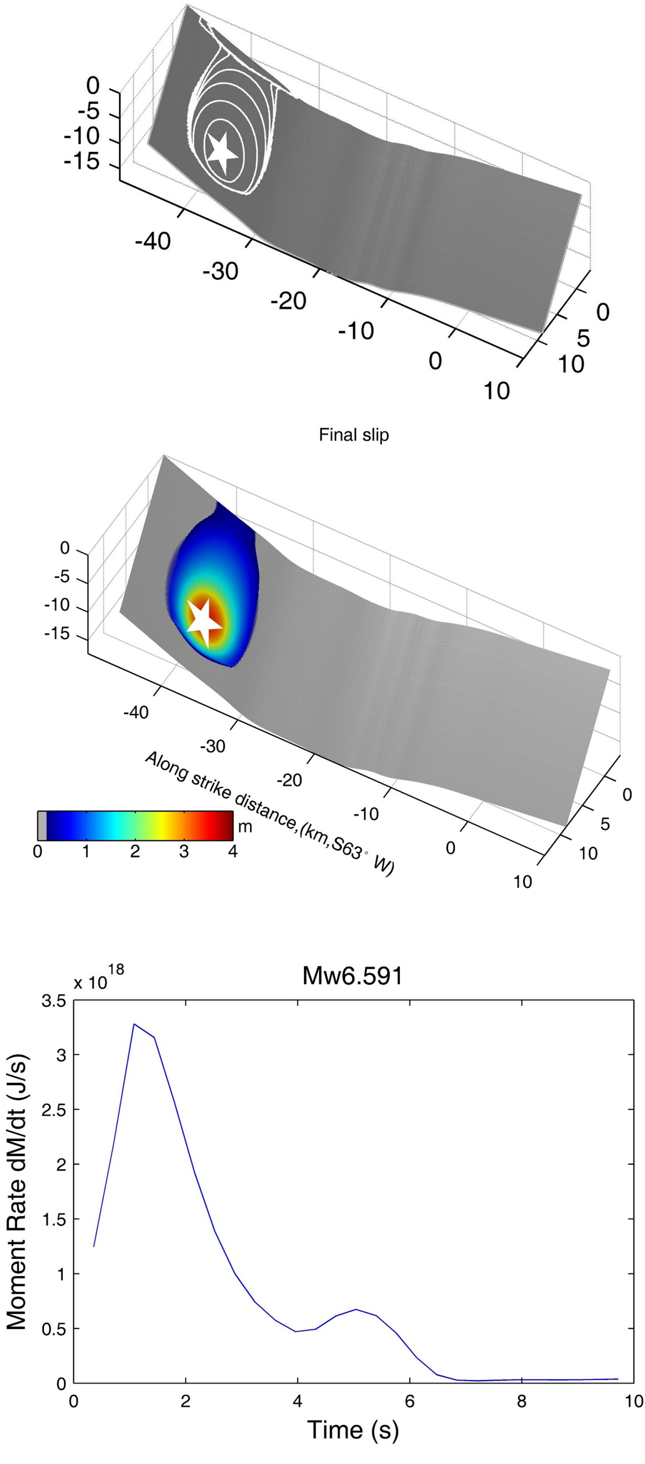
Final slip
Along strike distance,(km,S63° W)
m
Mw6.591
x 10^18
Moment Rate dM/dt (J/s)
Time (s)

Figure 8

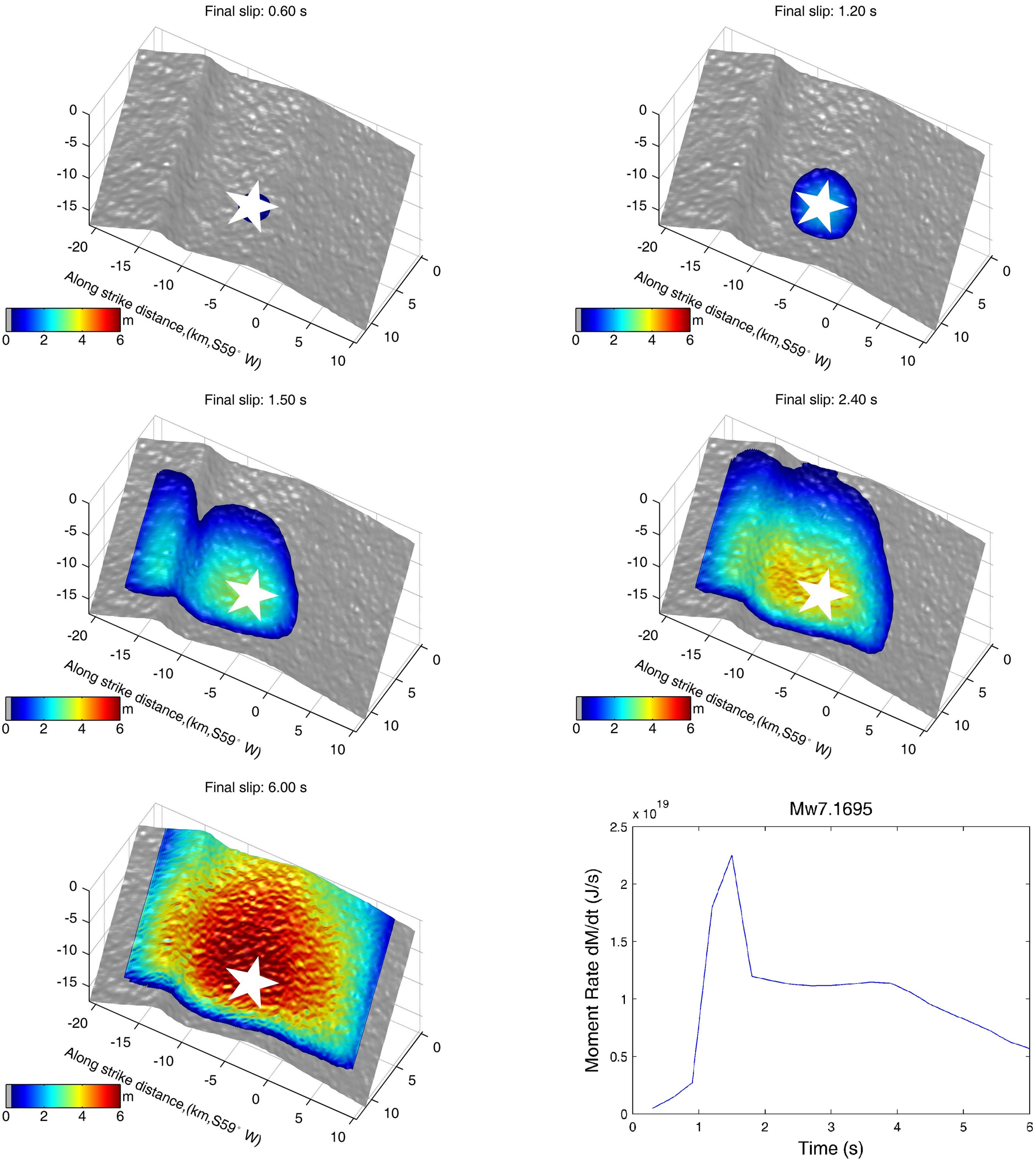

Final slip: 0.60 s
Final slip: 1.20 s
Final slip: 1.50 s
Final slip: 2.40 s
Final slip: 6.00 s
Along strike distance,(km,S59° W)
m
Mw7.1695
x 10^19
Moment Rate dM/dt (J/s)
Time (s)

Figure 9

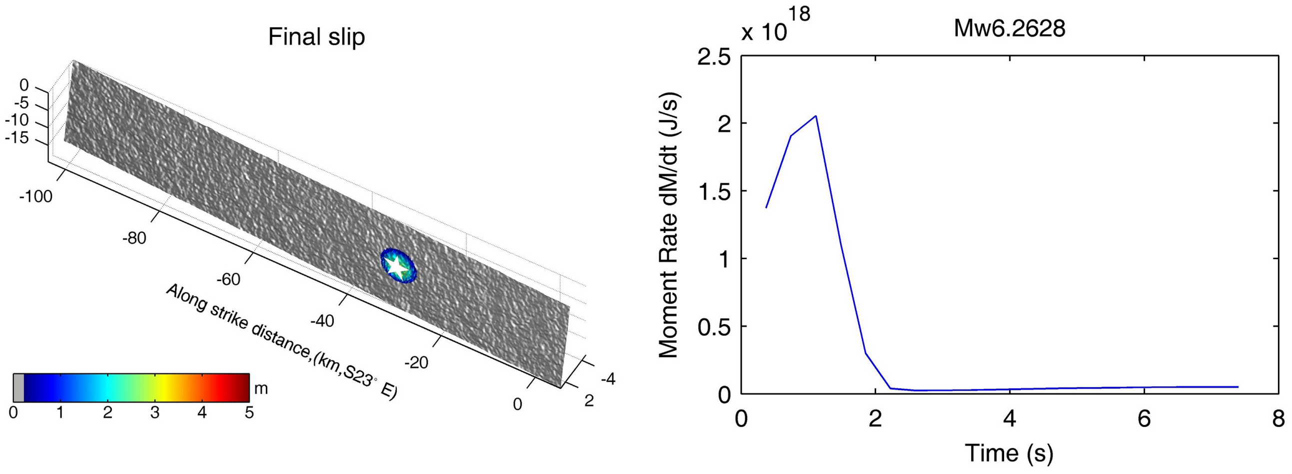
Final slip
0
-5
-10
-15
-100
-80
-60
-40
-20
0
-4
2
Along strike distance,(km,S23° E)
m
0
1
2
3
4
5
x 10^18
Mw6.2628
2.5
2
1.5
1
0.5
0
Moment Rate dM/dt (J/s)
0
2
4
6
8
Time (s)

Figure 10

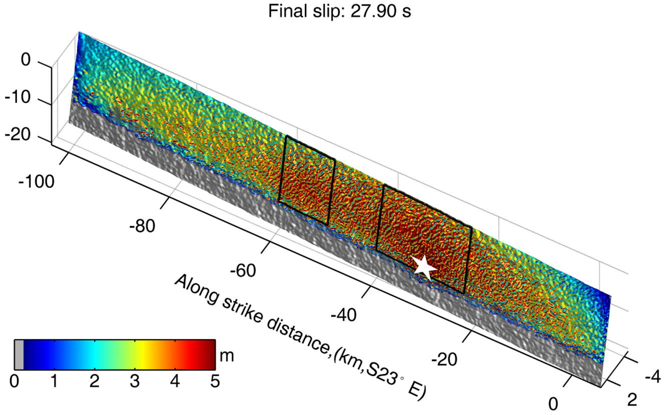
Final slip: 27.90 s
0
-10
-20
-100
-80
-60
-40
-20
0
Along strike distance,(km,S23° E)
-4
2
m
0
1
2
3
4
5

Figure 11

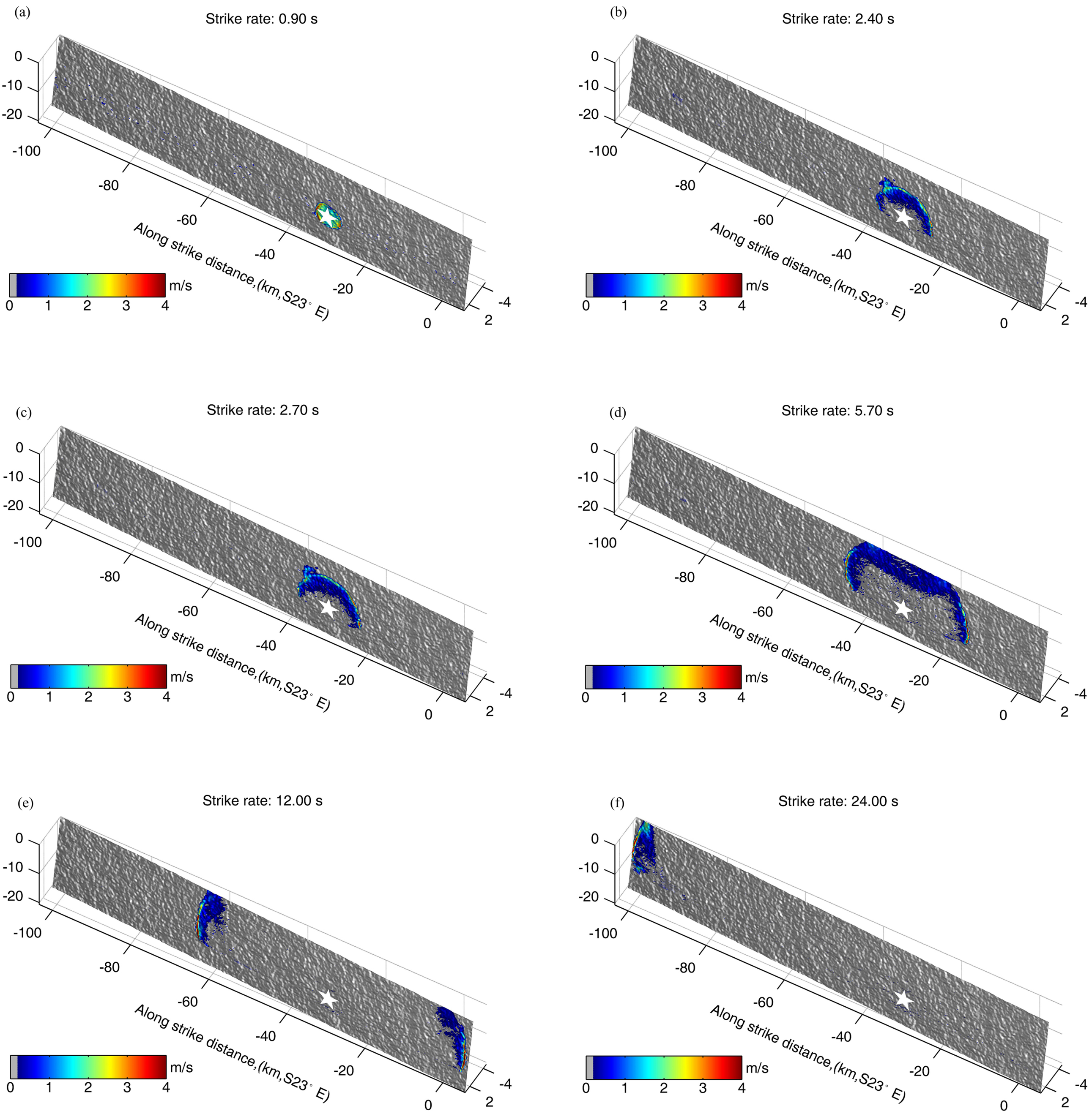

(a)
Strike rate: 0.90 s
(b)
Strike rate: 2.40 s
(c)
Strike rate: 2.70 s
(d)
Strike rate: 5.70 s
(e)
Strike rate: 12.00 s
(f)
Strike rate: 24.00 s
0
-10
-20
-100
-80
-60
-40
-20
0
-4
2
Along strike distance,(km,S23° E)
m/s
0 1 2 3 4

Figure 12

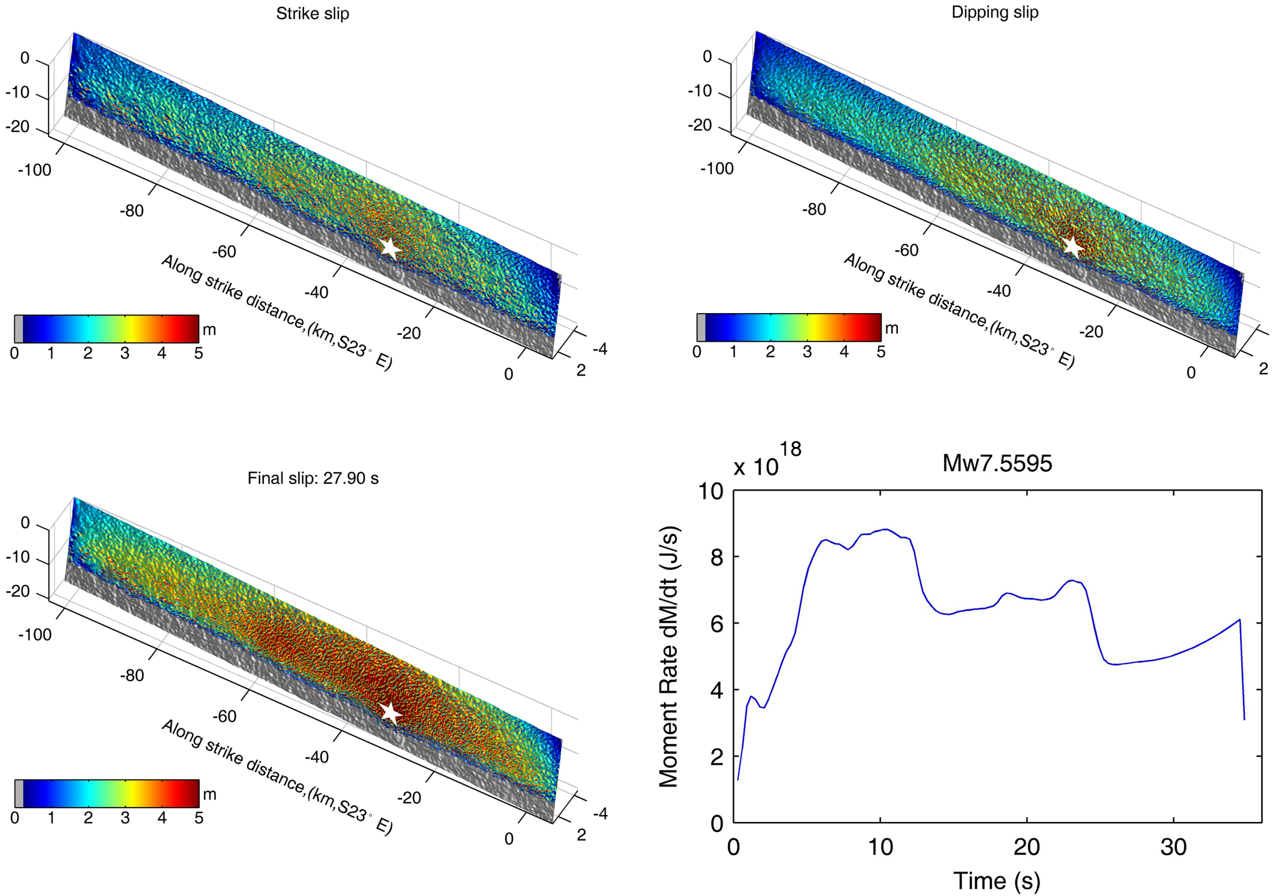

Strike slip
Dipping slip
Final slip: 27.90 s
Along strike distance,(km,S23° E)
m
Mw7.5595
x 10^18
Moment Rate dM/dt (J/s)
Time (s)

Figure 13

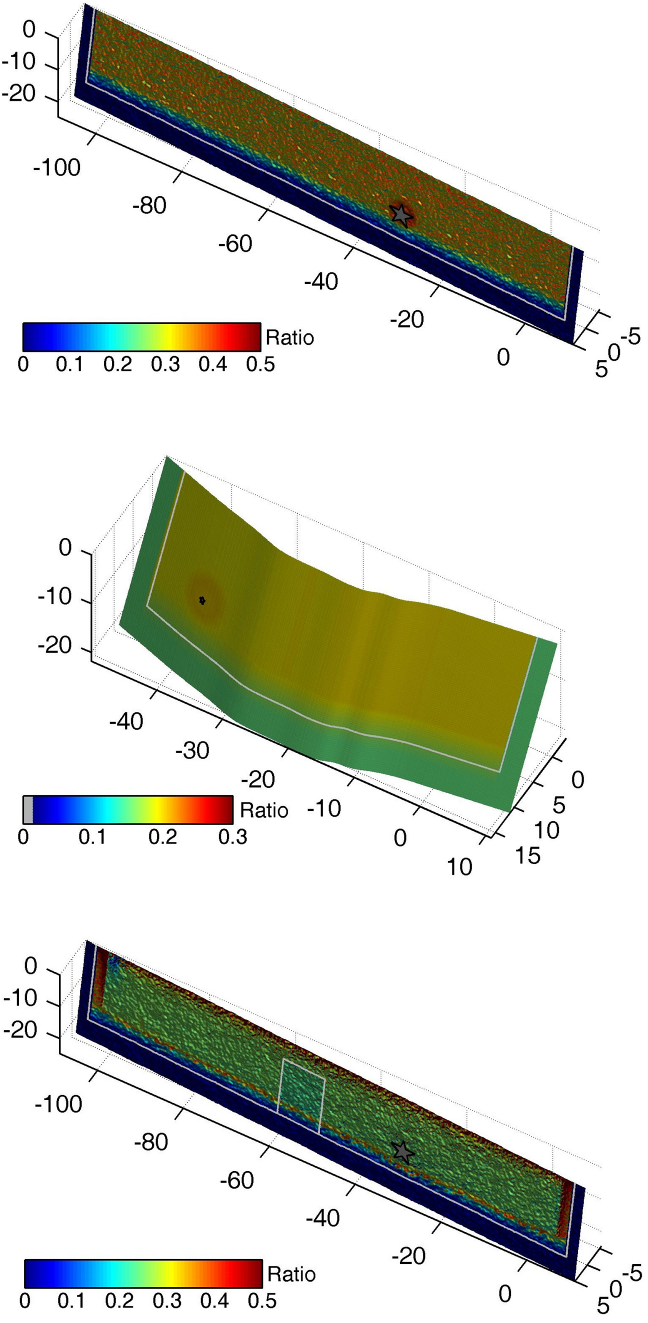

Ratio
0 0.1 0.2 0.3 0.4 0.5
0
-10
-20
-100
-80
-60
-40
-20
0
-5
0
5
Ratio
0 0.1 0.2 0.3
0
-10
-20
-40
-30
-20
-10
0
10
0
5
10
15
Ratio
0 0.1 0.2 0.3 0.4 0.5
0
-10
-20
-100
-80
-60
-40
-20
0
-5
0
5

Figure 14